APPLIED PHYSICS

On-demand spin-state manipulation of single-photon emission from quantum dot integrated with metasurface

Yanjun Bao[1]*, Qiaoling Lin[1]*, Rongbin Su[1], Zhang-Kai Zhou[1], Jindong Song[2], Juntao Li[1†], Xue-Hua Wang[1†]

The semiconductor quantum dot (QD) has been successfully demonstrated as a potentially scalable and on-chip integration technology to generate the triggered photon streams that have many important applications in quantum information science. However, the randomicity of these photon streams emitted from the QD seriously compromises its use and especially hinders the on-demand manipulation of the spin states. Here, by accurately integrating a QD and its mirror image onto the two foci of a bifocal metalens, we demonstrate the on-demand generation and separation of the spin states of the emitted single photons. The photon streams with different spin states emitted from the QD can be flexibly manipulated to propagate along arbitrarily designed directions with high collimation of the smallest measured beaming divergence angle of 3.17°. Our work presents an effectively integrated quantum method for the simultaneously on-demand manipulation of the polarization, propagation, and collimation of the emitted photon streams.

INTRODUCTION

The spin state of photon streams is one of the most important quantum resources. It not only provides test beds for the basic quantum principles, including Bell's inequalities (*1*), quantum nonlocality (*2*), Einstein-Podolsky-Rosen steering (*3*), and nonclassicality (*4*), but also has many important applications in quantum information science, such as quantum teleportation (*5*, *6*), quantum cryptography (*7*), quantum information transfer (*8*), and quantum entanglement (*9*). The semiconductor quantum dot (QD) is considered as an excellent single-photon source and has been successfully demonstrated as a potentially scalable and on-chip integration technology to generate the triggered and high-performance single-photon streams (*10*–*15*). However, the randomicity of these photon streams, i.e., the inherent omnidirectional and randomly polarized emission from the QD, seriously compromises its use. Although a great deal of efforts have been devoted to control the directional emission of the QDs by nanostructures (*16*–*20*), the on-demand generation of the spin single-photon streams with flexible propagation control and high collimation for the QD emission, which requires extremely complex multidimensional manipulations, has not yet been realized.

The metasurfaces are two-dimensional structures composed of subwavelength scattering elements that can flexibly manipulate the amplitude, phase, and polarization of light at nanoscale. They have emerged as promising materials for integration that enable flat optical components for a plethora of applications, including deflector (*21*), ultrathin metalens (*22*–*26*), holograms (*27*–*29*), vortex beam generation (*30*–*32*), etc. Recently, a few initiatives have been taken to use the metasurface in quantum optics, such as creating entanglement (*9*, *33*, *34*), detecting coherent perfect absorption of single photons (*35*), and imaging (*36*), suggesting it as a new platform for quantum optics. Although the spin-state control of plane-wave incident beam has been widely verified using metasurface (*37*, *38*), the spin manipulation of omnidirectional single-photon emission from a point source (such as QD) has not yet been addressed.

Here, we demonstrate an on-demand spin-state generation of the single-photon streams with arbitrary propagation control and high collimation by accurately integrating the QD and its mirror image on the two foci of a spin-splitting bifocal metalens (SSBM). The designed device is illustrated in Fig. 1A, where a QD is embedded in the center dielectric layer of a metal-dielectric-metalens structure, and its emission can be reflected by the metal and then manipulated by the metalens. The control performance of the device is sensitive to the position of QD relative to the metalens, and the key to success is to make the QD and its mirror image accurately overlap with the two foci of the SSBM. To place the QD exactly at the focal position, we adopt fluorescence imaging technology, which can achieve a high overlay accuracy of ~30 nm. We experimentally demonstrate the generation and splitting of spin-state single-photon emissions with different designed propagation directions. The obtained smallest observed beaming divergence angle of the emission is 3.17.

RESULTS

Figure 1A shows a schematic view of our designed QD-metasurface–integrated device for on-demand manipulation of the single-photon emission from a QD. The QD is embedded in a homogeneous dielectric layer (SiO_2), which is sandwiched between a gold mirror and silicon metasurface. The gold mirror at the bottom is used to reflect the QD emission upward to the metasurface, therefore improving the collection efficiency. Although the emission of QD is randomly polarized, it can always be decomposed into left and right circular polarizations (LCP and RCP). To split the two opposite spin-state emissions along different directions, we use the concept of Pancharatnam-Berry phase, which can introduce an abrupt geometric phase change upon the light after passing through the metasurface.

[1]State Key Laboratory of Optoelectronic Materials and Technologies, School of Physics, Sun Yat-sen University, Guangzhou 510275, China. [2]Center for Opto-Electronic Materials and Devices Research, Post-Si Semiconductor Institute, Korea Institute of Science and Technology, Seoul 02-791, South Korea.
*These authors contributed equally to this work.
†Corresponding author. Email: lijt3@mail.sysu.edu.cn (J.L.); wangxueh@mail.sysu.edu.cn (X.-H.W.)

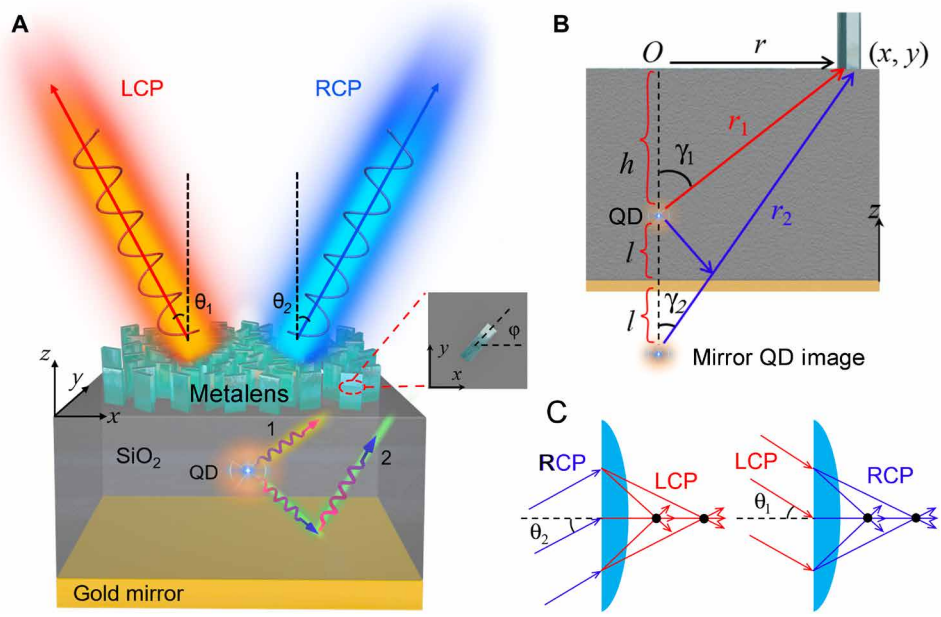

Fig. 1. Design of metasurface for on-demand spin-state control of single-photon emission. (**A**) Illustration of the designed structure for manipulating QD emission. The structure consists of three layers: a top metasurface layer, a middle dielectric layer with a QD embedded, and a bottom gold reflector layer. The metasurface is designed to convert the QD emissions from the two paths (labeled by 1 and 2) into two opposite circularly polarized beams that propagate along the directions with angles of θ_1 and θ_2 relative to the surface normal of metasurface, respectively. The inset shows the top view of a silicon nanoblock with a rotation angle of φ. (**B**) Side view of relative positions of QD and silicon nanoblock. r_1 (r_2) is the distance from the silicon nanoblock $r(x, y)$ to the QD (mirror QD image), and $\gamma_1(\gamma_2)$ is the angle between the direction r_1 (r_2) and z axis. h and l are the vertical distances from the QD to the metasurface and the gold mirror, respectively. (**C**) Schematic of the equivalent two-focus metalens of the metasurface. The LCP and RCP illuminated at incident angles of θ_1 and θ_2 can be focused into the same two foci.

In detail, the metasurface is composed of anisotropic dielectric nanoblocks with orientation function $\varphi(x, y)$ (Fig. 1A), which can generate a local geometric phase of $\pm 2\varphi(x, y)$, where the sign is determined by the combination of the incidence/transmission polarizations, with a + sign for RCP/LCP and a − sign for LCP/RCP. With proper design, the LCP and RCP polarizations of QD emissions can be converted into their respective opposite circularly polarized beams and propagate along independent desired directions (denoted by angles of θ_1 and θ_2 relative to the device surface normal for LCP and RCP beams). Here, it is worth mentioning the difference with conventional spin-splitting metasurface under plane-wave illumination (*37*, *38*). For example, in the plane-wave incidence situation, if the transmitted circularly polarized beam is designed to diffract at an angle θ with respect to incident axis, then the one with opposite circular polarization will automatically be diffracted to the mirror-symmetric direction with an angle −θ once the circular polarization of the incident beams is reversed. However, such automatic spin splitting is not suitable for point source illumination as in here because of the varied optical paths from the point source to the different positions of the metasurface. Therefore, we propose a new design strategy to independently manipulate the two opposite circularly polarized beams so that they can propagate into arbitrary directions (not limited to $\theta_1 = -\theta_2$). Moreover, both the QD emissions that are emitted in a straight line to the metasurface (labeled as 1 in Fig. 1A) and reflected by the gold mirror (labeled as 2 in Fig. 1A) should be taken into account in the design of metasurface. To realize such functionality, the geometric orientation angle φ and its corresponding position (x, y) of each nanoblock can be derived by solving the following simultaneous equations (see details in the Supplementary Materials)

$$\begin{cases} -2\varphi + \arg\left[\frac{\cos(\gamma_1)}{r_1}\exp(i2\pi n r_1/\lambda) - \frac{\cos(\gamma_2)}{r_2}\exp(i2\pi n r_2/\lambda)\right] = 2\pi\sin(\theta_1)\,x/\lambda + 2p\pi \\ +2\varphi + \arg\left[\frac{\cos(\gamma_1)}{r_1}\exp(i2\pi n r_1/\lambda) - \frac{\cos(\gamma_2)}{r_2}\exp(i2\pi n r_2/\lambda)\right] = 2\pi\sin(\theta_2)\,x/\lambda + 2q\pi \end{cases} \quad (1)$$

where r_1 (r_2) is the distance from the silicon nanoblock $r(x, y)$ to the QD (mirror QD image), $\gamma_1(\gamma_2)$ is the angle between the direction r_1 (r_2) and z axis (Fig. 1B), λ is the emitted wavelength of the QD, n is the refractive index of dielectric layer, arg is the argument of complex number, and p and q are two integers. From the above equation, one can note that both the emissions from the QD and mirror image positions with the same circular polarization can be guided into the same direction. The resulting metasurface can be equivalent to a bifocal metalens, which can focus the LCP and RCP lights with different incident angles (Fig. 1C). Therefore, we refer this metasurface structure to as SSBM.

For the QD emission with no polarization change after passing through the SSBM (LCP to LCP or RCP to RCP), it undergoes no phase change and will add background noise in the transmitted field. Therefore, it is necessary to maximize the conversion efficiency to the opposite circular polarization (LCP to RCP or vice versa) for the single silicon nanoblock unit in the SSBM. Considering the big range of emission wavelengths from different QD samples and the spectra shifts caused by the complex fabrication process (see details in the following fabrication process), the geometry dimensions of the silicon

nanoblock are optimized to exhibit a large conversion efficiency over a broadband wavelength domain (880 to 950 nm). For an optimized silicon nanoblock standing on a SiO_2 substrate with a width of 140 nm, a length of 280 nm, and a height of 600 nm, the simulated conversion efficiency is able to realize more than 85% in the wavelength range of interest (fig. S2). If optimized for only one particular wavelength, more than 97% efficiency can be obtained. One prerequisite of such high conversion efficiency is that there is a large difference of refractive index between the silicon SSBM and the SiO_2 substrate. If the SSBM and the substrate (i.e., the center dielectric layer of the device) have the same materials, then the fabrication of the device in Fig. 1 would be simpler, but the efficiency cannot be high.

The beam divergence is the key parameter to estimate the collimation of the device. For a normal beam, the divergence angle is inversely proportional to the diameter of the beam. This conclusion is valid under the assumption that the beam output port satisfies the equal-amplitude condition. However, since the QD emits as a point source, the amplitude of the scattered field on the SSBM is not homogeneous but decays as $(r^2 + h^2)^{-1/2}$, where r is the distance to the center of SSBM and h is the one from the center of SSBM to the position of QD. Therefore, only a finite area around the center of SSBM can effectively contribute to the collimation of the beam. Increasing h can increase the effective area and lead to the reduction of the beam divergence angle (fig. S3). However, on the other hand, a larger h also increases the leakage loss of the QD radiation along the dielectric waveguide (fig. S4) as well as the difficulty to identify the overlay markers for locating the position of QD and SSBM fabrication in the experiment (see the following fabrication process). We hence choose a balance value of h = 2 μm in both simulation and experiment. The distance of the QD to the metallic mirror l is set as 1 μm.

To demonstrate the functionalities of our design SSBM, we consider the two scattered spin-state (LCP and RCP) beams to propagate symmetrically in the two sides with respect to the surface normal, and without loss of generality, we verify the two cases with $\theta_1 = \theta_2 = 0°$ (device 1) and $\theta_1 = -\theta_2 = 20°$ (device 2) by a full-wave numerical simulation (see fig. S2 for the metasurface structure pattern). The simulation results of a different case with $\theta_1 = -\theta_2 = 10°$ is also shown in fig. S2. In the simulation, the QD is represented as an electric dipole polarized along the x direction and emitted at a wavelength of 910 nm. Limited by the calculation power, the diameter of the SSBM is set to be 12 μm, which can collect the QD emissions in the range of angles corresponding to a numerical aperture (NA) = 0.95 for the straightly scattered emission and NA = 0.83 for the reflected emission.

For device 1 (Fig. 2A), as we expect, the total scattered far field propagates in the direction along the surface normal. The LCP and RCP components of the scatterings coincide spatially with almost the same intensities. The anisotropy of the far-field intensity at the center is related primarily to the electric dipole direction in the simulation. To characterize the collimation of the beam, the divergence angle is evaluated by measuring its full width at half maximum (FWHM) of the scattering far-field pattern, which is about 5.8° at maximum. The SSBM plays the main role in narrowing the scattering angles in the far field. As a comparison, if without the top layer of SSBM, the QD emission spreads over a wide range of directions in the upper hemisphere (fig. S4). We also consider a structure without the gold mirror and find that the peak value of the scattering intensity is about half of the one with complete structure (fig. S4).

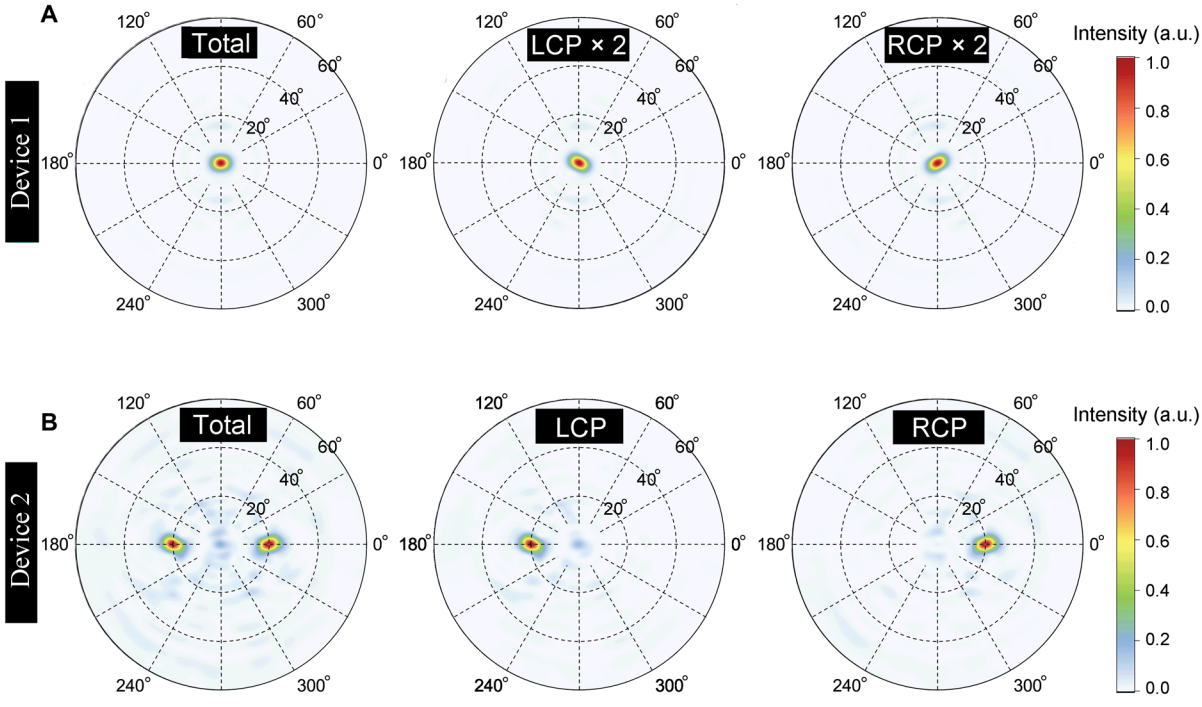

Fig. 2. Simulated results of the far-field pattern of devices 1 and 2. (**A** and **B**) Calculated total and LCP and RCP intensities of the far-field scattering patterns for devices 1 (A) and 2 (B), respectively. The total intensity is the sum of LCP and RCP components. Note that the intensities of LCP and RCP in device 1 are multiplied by 2 to use the same color bar with the total far-field intensity. a.u., arbitrary units.

This clearly shows the role of gold mirror in improving the collection efficiency of the QD emission. For the complete structure, the collection efficiency within NA = 0.65 (the same value used in the experiment) is calculated around 32%. By increasing the diameter of SSBM, the collection efficiency can be further increased but ultimately becomes saturated because of the energy loss dissipated along the dielectric waveguide and absorbed by silicon SSBM and gold mirror. Although designed at single wavelength of 910 nm, the device has a robust performance in controlling the QD emission within a broadband wavelength of 880 to 950 nm (fig. S5). For another device 2 (Fig. 2B), the simulated far-field patterns show that the LCP and RCP scattered lights can be separated spatially and propagate in the directions with azimuthal angles 0° and 180°, respectively, with both having the same radial angle of 20°, which is exactly the same as the one that we designed. The maximal FWHM divergence angle of the two beams is about 6.7° for this case. Note that the emission patterns are not symmetric, which is due to the asymmetry of the designed SSBM structure (see fig. S2). There always exist residual emissions along other directions; however, because of the large emission intensity at the designed angle ±20°, these residual emissions are not obvious.

The fabrication process of the device is illustrated in Fig. 3. First, a 1-μm-thick $Al_{0.7}Ga_{0.3}As$ sacrificial layer is grown on a GaAs substrate, followed by a 160-nm-thick GaAs membrane that consists of a single layer of InAs QDs by molecular beam epitaxy (see Materials and Methods; Fig. 3A). Next, 1-μm thickness of SiO_2 layer was deposited on the surface of the wafer followed by e-beam evaporation of 1-nm-thick Ti adhesion layer and 100-nm-thick reflective Au layer (Fig. 3B). By spinning and ultraviolet-curing adhesive NOA61 (Norland Products Inc.), the wafer was bonded to a transparent glass (Fig. 3C). Then, the GaAs substrate and $Al_{0.7}Ga_{0.3}As$ sacrificial layer are removed through selective wet-etching process, with the GaAs membrane left at the top (Fig. 3D).

Because the QD is designed to be embedded in a homogeneous dielectric layer in our designed structure, the materials around the InAs QD should be removed and replaced with SiO_2. To do this, we first prepare the gold alignment markers on the GaAs membrane, which can achieve a high overlay accuracy of ~30 nm. Through the fluorescence imaging technology (*39*), the relative positions of the QD and alignment markers can be entirely determined. Next, electron beam lithography (Raith EBPG 5000 Plus) and inductively coupled plasma etching (Wavetest PlasmaPro System 100ICP180) are applied to remove the materials around the QD, which leads to a GaAs nanopillar (radius of about 150 to 200 nm) with an InAs QD embedded (Fig. 3E). To remove the surface unevenness caused by the GaAs nanopillar, hydrogen silsesquioxane was spin-coated to improve the smoothness via annealing. Then, 2-μm-thick SiO_2 and 600-nm-thick amorphous silicon are deposited on the sample (Fig. 3F). Note that the thickness of the deposited SiO_2 layer cannot be too thick, otherwise it will be hard to identify the gold markers underneath the SiO_2 layer for SSBM fabrication because of its poor electrical conductivity of SiO_2. Last, similar to the nanopillar fabrication process, the silicon SSBM structure with a diameter of 30 μm is patterned at the top layer with its center vertically overlapping the position of QD (Fig. 3G). The optical and scanning electron microscopy images of the fabricated SSBM structure are shown in Fig. 3 (H and I).

In the fabricated structure, the QD is embedded in a GaAs nanopillar surround by a homogeneous dielectric layer, which is somewhat

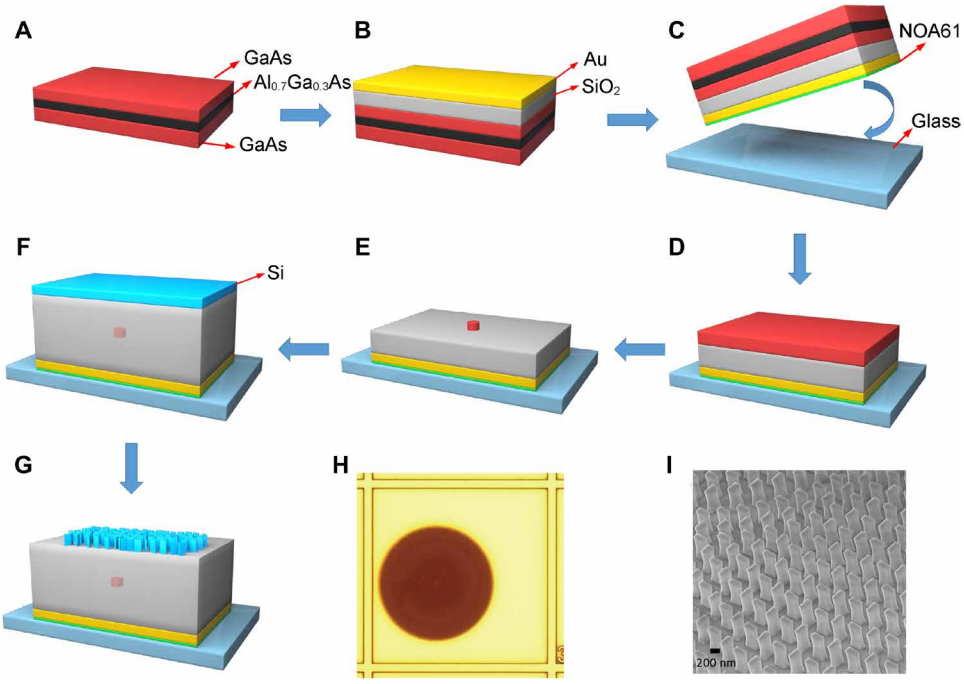

Fig. 3. Fabrication process of the integrated QD-SSBM device. (**A**) A wafer with an InAs QD embedded grown by molecular beam epitaxy. (**B**) Deposition of SiO_2 dielectric layer and gold mirror. (**C**) Wafer bonding with fused glass with adhesive NOA61. (**D**) Removing of GaAs substrate and $Al_{0.7}Ga_{0.3}As$ sacrificial layer by selective wet-etching process. (**E**) Fabrication of GaAs nanopillar with an InAs QD embedded. (**F**) Deposition of SiO_2 and amorphous silicon layer. (**G**) Fabrication of SSBM structure on the silicon layer using electron beam lithography. (**H**) Optical image of the fabricated SSBM and the gold marks. (**I**) Scanning electron microscopy image of the fabricated SSBM.

different with the designed one. To understand the influence of the GaAs nanopillar on the device functionalities, the far-field scattering pattern is numerically investigated, which shows only slight changes with the one from the designed structure when the radius of GaAs nanopillar is not greater than 200 nm (fig. S6). The reason may be that the emitted wavelength of QD is much larger than the size of the nanopillar, which can still be considered as a point source.

We set up an optical measurement system to measure the far-field scattering patterns of the devices (see Materials and Methods). A 785-nm laser is used to excite the photoluminescence (PL) of the InAs QD, which is then collected by an objective with NA = 0.65. The Fourier plane is imaged onto a charge-coupled device (CCD) camera to measure the scattering angles of QD. In addition, a quarter-wave plate (QWP) and a linear polarizer are used to distinguish the LCP and RCP components of the emission.

Figure 4A displays the measured Fourier image of the total emission from InAs QD for device 1. A single bright spot can be observed in the center of the emission pattern. To definitely estimate the divergence angle of the beam, the CCD pixels are translated to the corresponding scattering angles (fig. S7). By Lorentz fitting the line plot across the center peak, the FWHMs of the divergence angle are obtained as 5.47° and 5.99° along the horizontal and vertical directions, respectively. We also fabricated a device without the top SSBM, and the measured result shows an omnidirectional scattering that covers a large angular range in the far-field emission pattern (fig. S8). The collection efficiency of the device 1 is measured as about 25%. This value is smaller than the simulated one (32%) because of the possible imperfect fabrication of the SSBM structure, the alignment error of the QD, and the blinking of the QD after the fabrication of the GaAs nanopillar (*39*).

Figure 4B shows the measured results of another device 2. For the scattering with linear polarization selection (the axes of QWP and linear polarizer are parallel), the emission pattern exhibits two bright spots located at scattering angles of ±17.62°. The scattering angles are slightly different with the designed values ±20°, which may be caused by the deviation of the emitted wavelength and position location error of QD (figs. S5 and S9). Through the polarization analysis (rotating the fast axis of QWP at an angle of ±45° relative to that of linear polarizer), we can further verify that the two bright spots are indeed LCP and RCP, with measured degree of polarization with 0.88 and 0.78, respectively [defined as $(I_{max} - I_{min})/(I_{max} + I_{min})$, where I is the integrated intensity of LCP and RCP spots with the integral radius equaling to the FWHM. The integrated intensity of LCP and RCP spots is almost equal, indicating that the emission of the QD is nearly linearly polarized. The measured FWHMs along the horizontal direction for the two beams are 4.83° and 3.17°, respectively, which are unexpectedly better than the simulation result (6.7°). We attribute this anomaly to the fact that the SSBM used in the experiment has a much larger diameter, which increases the directionality.

Last, it is worth verifying whether the QD emission in the designed device is at a single-photon state. We perform the second-order correlation function measurement (see Materials and Methods) of device 1 at a wavelength of 879.903 nm (fig. S10), with a $g^{(2)}(0)$ value of 0.200 ± 0.013 (Fig. 5) that well exhibits single-photon characteristics. This result demonstrates the purity of QD single-photon emission and suggests our SSBM structure as a new powerful platform for the manipulation of single-photon emissions.

DISCUSSION

In summary, we have proposed and experimentally demonstrated a SSBM structure that is integrated with QD for the on-demand control of single-photon emissions. The QD and its mirror image are accurately placed at the two foci of the SSBM with the assistance of fluorescence imaging technology. The flexibility of metasurface design enables us to split the different spins of single-photon emissions with arbitrary propagation control and high collimation. Because of the varied propagation phases from the QD to the metasurface, the two opposite spin-state emissions can be independently manipulated, which stands in contrast to previous metasurfaces designed under plane-wave incidence that have interrelated functionalities for the

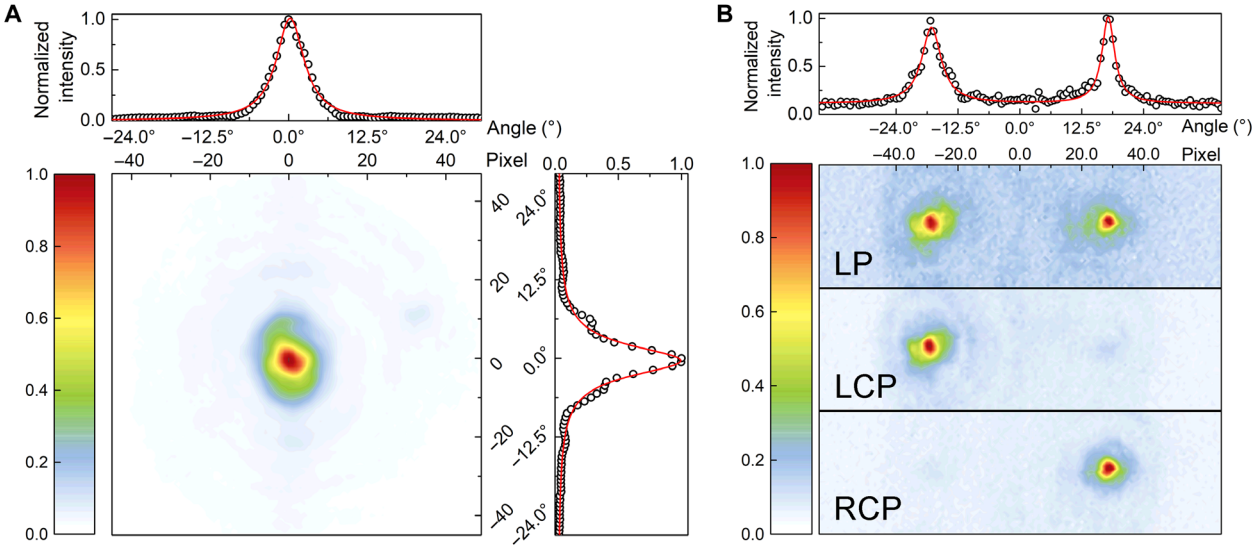

Fig. 4. Measured far-field patterns of devices 1 and 2. (**A**) Measured Fourier image of the total far-field QD emission for device 1. (**B**) Measured Fourier image of the linear polarization (LP) and LCP and RCP far-field intensities of QD emission for device 2. The red solid lines are the Lorentz fitting of the line plot across the scattering peaks along the horizontal and vertical directions.

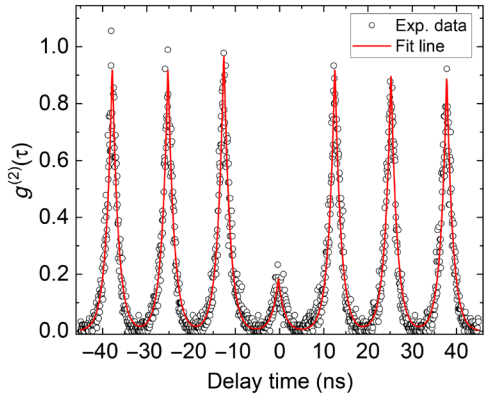

Fig. 5. Measured second-order correlation function $g^{(2)}(\tau)$ of the QD emission after the fabrication of GaAs nanopillar and SSBM. The black open circles show the measured results. The red line is the fitting curve using the model in (*40*). This value of $g^{(2)}(0)$ is calculated from the integrated area in the zero-delay peak divided by the average area of other peaks away from zero delay. The uncertainty value is given by propagation of the SD in the peak fitting.

two spin-state lights. The proposed strategy for manipulating the QD emission with metasurface can be extended to control other degrees of freedom of light, such as the orbit angular momentum (OAM), which may have applications in spin-OAM entanglement. We anticipate that further research toward the QD-metasurface interaction can enable the development of other novel devices, such as QD single-photon hologram, QD emission focusing, etc.

MATERIALS AND METHODS

Growth and optical properties of QDs

The sample was grown in a molecular beam epitaxy system equipped with an ion getter pump and a cryogenic pump. After oxide removal of a semi-insulating (001) GaAs wafer at the substrate temperature of 600°C under As tetramer ambient, a 300-nm-thick GaAs buffer, a 1000-nm-thick AlGaAs of 70% Al composition, and a 85-nm-thick GaAs layer were grown successively at 590°C. Low-density InAs QDs were grown on it. Another 85-nm-thick GaAs capping layer was deposited to cover the QDs. The film was thermally treated in the main chamber at 600°C under As ambient. The density of QDs was founded as less than one QD cluster per 50 μm by 50 μm, and a cluster may have a few QDs inside it (fig. S10). The QDs PL spectra of devices 1 and 2 are also measured (fig. S10). The lifetime of the QD emission is 1.35 ns, which is obtained from the fitting parameters of the second-order correlation function in Fig. 5.

Optical measurement

The samples were mounted on the cold head of a closed-cycle helium cryostat and cooled down to ~4 K. For the PL measurement, a 785-nm continuous-wave laser with a linear polarization was coupled into a single-mode fiber. The pumping power was adjusted using a neutral density filter before excitation. The excitation power was ~2.5 μW. The emission was collected using a 50× objective with an NA of 0.65 (LCPLN50XIR, Olympus). Two lenses (f = 400 mm and f = 200 nm) were used to image the Fourier space plane onto a liquid nitrogen–cooled silicon CCD. The LCP and RCP polarization of the emission were measured by using a QWP followed by a linear polarizer. A detail of the optical setup for scattering measurement is shown in fig. S7.

The second-order correlation function was measured using the Hanbury Brown and Twiss interferometer. Excitation was performed via a 780-nm pulsed Ti:sapphire laser with a 79-MHz repetition rate, 100-fs pulse width, and 1.5-μW power. The signal was equally divided with a beam splitter, detected by two single-photon detectors, and recorded by a time-correlated single-photon counting system (PicoHarp300, PicoQuant).

SUPPLEMENTARY MATERIALS

Supplementary material for this article is available at http://advances.sciencemag.org/cgi/content/full/6/31/eaba8761/DC1

REFERENCES AND NOTES

1. A. Aspect, J. Dalibard, G. Roger, Experimental test of Bell's inequalities using time-varying analyzers. *Phys. Rev. Lett.* **49**, 1804 (1982).
2. J. W. Pan, D. Bouwmeester, M. Daniell, H. Weinfurter, A. Zeilinger, Experimental test of quantum nonlocality in three-photon Greenberger-Horne-Zeilinger entanglement. *Nature* **403**, 515–519 (2000).
3. D. J. Saunders, S. J. Jones, H. M. Wiseman, G. J. Pryde, Experimental EPR-steering using Bell-local states. *Nat. Phys.* **6**, 845–849 (2010).
4. R. Lapkiewicz, P. Li, C. Schaeff, N. K. Langford, S. Ramelow, M. Wieśniak, A. Zeilinger, Experimental non-classicality of an indivisible quantum system. *Nature* **474**, 490–493 (2011).
5. D. Bouwmeester, J.-W. Pan, K. Mattle, M. Eibl, H. Weinfurter, A. Zeilinger, Experimental quantum teleportation. *Nature* **390**, 575 (1997).
6. X.-L. Wang, X.-D. Cai, Z.-E. Su, M.-C. Chen, D. Wu, L. Li, N.-L. Liu, C.-Y. Lu, J.-W. Pan, Quantum teleportation of multiple degrees of freedom of a single photon. *Nature* **518**, 516–519 (2015).
7. E. Waks, K. Inoue, C. Santori, D. Fattal, J. Vuckovic, G. S. Solomon, Y. Yamamoto, Secure communication: Quantum cryptography with a photon turnstile. *Nature* **420**, 762–762 (2002).
8. E. Nagali, F. Sciarrino, F. De Martini, L. Marrucci, B. Piccirillo, E. Karimi, E. Santamato, Quantum information transfer from spin to orbital angular momentum of photons. *Phys. Rev. Lett.* **103**, 013601 (2009).
9. T. Stav, A. Faerman, E. Maguid, D. Oren, V. Kleiner, E. Hasman, M. Segev, Quantum entanglement of the spin and orbital angular momentum of photons using metamaterials. *Science* **361**, 1101–1103 (2018).
10. J. Liu, R. Su, Y. Wei, B. Yao, S. F. C. da Silva, Y. Yu, J. Iles-Smith, K. Srinivasan, A. Rastelli, J. Li, X. Wang, A solid-state source of strongly entangled photon pairs with high brightness and indistinguishability. *Nat. Nanotechnol.* **14**, 586–593 (2019).
11. A. J. Shields, Semiconductor quantum light sources. *Nat. Photonics* **1**, 215–223 (2007).
12. J. Claudon, J. Bleuse, N. S. Malik, M. Bazin, P. Jaffrennou, N. Gregersen, C. Sauvan, P. Lalanne, J.-M. Gérard, A highly efficient single-photon source based on a quantum dot in a photonic nanowire. *Nat. Photonics* **4**, 174–177 (2010).
13. C. Matthiesen, A. N. Vamivakas, M. Atature, Subnatural linewidth single photons from a quantum dot. *Phys. Rev. Lett.* **108**, 093602 (2012).
14. P. Lodahl, A. F. Van Driel, I. S. Nikolaev, A. Irman, K. Overgaag, D. Vanmaekelbergh, W. L. Vos, Controlling the dynamics of spontaneous emission from quantum dots by photonic crystals. *Nature* **430**, 654–657 (2004).
15. P. Senellart, G. Solomon, A. White, High-performance semiconductor quantum-dot single-photon sources. *Nat. Nanotechnol.* **12**, 1026–1039 (2017).
16. S. Morozov, M. Gaio, S. A. Maier, R. Sapienza, Metal-dielectric parabolic antenna for directing single photons. *Nano Lett.* **18**, 3060–3065 (2018).
17. A. G. Curto, G. Volpe, T. H. Taminiau, M. P. Kreuzer, R. Quidant, N. F. van Hulst, Unidirectional emission of a quantum dot coupled to a nanoantenna. *Science* **329**, 930–933 (2010).
18. T. Coenen, E. J. R. Vesseur, A. Polman, A. F. Koenderink, Directional emission from plasmonic yagi-uda antennas probed by angle-resolved cathodoluminescence spectroscopy. *Nano Lett.* **11**, 3779–3784 (2011).
19. N. Livneh, M. G. Harats, D. Istrati, H. S. Eisenberg, R. Rapaport, Highly directional room-temperature single photon device. *Nano Lett.* **16**, 2527–2532 (2016).
20. E. Johlin, S. A. Mann, S. Kasture, A. F. Koenderink, E. C. Garnett, Broadband highly directive 3D nanophotonic lenses. *Nat. Commun.* **9**, 4742 (2018).
21. Z. Zhou, J. Li, R. Su, B. Yao, H. Fang, K. Li, L. Zhou, J. Liu, D. Stellinga, C. P. Reardon, T. F. Krauss, X. Wang, Efficient silicon metasurfaces for visible light. *ACS Photonics* **4**, 544–551 (2017).
22. S. Wang, P. C. Wu, V.-C. Su, Y.-C. Lai, M.-K. Chen, H. Y. Kuo, B. H. Chen, Y. H. Chen, T.-T. Huang, J.-H. Wang, R.-M. Lin, C.-H. Kuan, T. Li, Z. Wang, S. Zhu, D. P. Tsai, A broadband achromatic metalens in the visible. *Nat. Nanotechnol.* **13**, 227–232 (2018).

23. Y. Bao, Q. Jiang, Y. Kang, X. Zhu, Z. Fang, Enhanced optical performance of multifocal metalens with conic shapes. *Light Sci. Appl.* **6**, e17071 (2017).
24. H. Liang, Q. Lin, X. Xie, Q. Sun, Y. Wang, L. Zhou, L. Liu, X. Yu, J. Zhou, T. F. Krauss, J. Li, Ultrahigh numerical aperture metalens at visible wavelengths. *Nano Lett.* **18**, 4460–4466 (2018).
25. M. Khorasaninejad, F. Capasso, Metalenses: Versatile multifunctional photonic components. *Science* **358**, eaam8100 (2017).
26. L. Du, Z. Xie, G. Si, A. Yang, C. Li, J. Lin, G. Li, H. Wang, X. Yuan, On-chip photonic spin hall lens. *ACS Photonics* **6**, 1840–1847 (2019).
27. W. T. Chen, K.-Y. Yang, C.-M. Wang, Y.-W. Huang, G. Sun, I.-D. Chiang, C. Y. Liao, W.-L. Hsu, H. T. Lin, S. Sun, L. Zhou, A. Q. Liu, D. P. Tsai, High-efficiency broadband meta-hologram with polarization-controlled dual images. *Nano Lett.* **14**, 225–230 (2014).
28. G. Zheng, H. Mühlenbernd, M. Kenney, G. Li, T. Zentgraf, S. Zhang, Metasurface holograms reaching 80% efficiency. *Nat. Nanotechnol.* **10**, 308–312 (2015).
29. Y. Bao, Y. Yu, H. Xu, C. Guo, J. Li, S. Sun, Z.-K. Zhou, C.-W. Qiu, X.-H. Wang, Full-colour nanoprint-hologram synchronous metasurface with arbitrary hue-saturation-brightness control. *Light Sci. Appl.* **8**, 95 (2019).
30. F. Yue, D. Wen, C. Zhang, B. D. Gerardot, W. Wang, S. Zhang, X. Chen, Multichannel polarization-controllable superpositions of orbital angular momentum states. *Adv. Mater.* **29**, 1603838 (2017).
31. G. Li, L. Wu, K. F. Li, S. M. Chen, C. Schlickriede, Z. Xu, S. Huang, W. Li, Y. Liu, E. Y. B. Pun, T. Zentgraf, K. W. Cheah, Y. Luo, S. Zhang, Nonlinear metasurface for simultaneous control of spin and orbital angular momentum in second harmonic generation. *Nano Lett.* **17**, 7974–7979 (2017).
32. Y. Bao, J. Ni, C.-W. Qiu, A minimalist single-layer metasurface for arbitrary and full control of vector vortex beams. *Adv. Mater.* **32**, 1905659 (2020).
33. P. K. Jha, N. Shitrit, J. Kim, X. Ren, Y. Wang, X. Zhang, Metasurface-mediated quantum entanglement. *ACS Photonics* **5**, 971–976 (2018).
34. K. Wang, J. G. Titchener, S. S. Kruk, L. Xu, H.-P. Chung, M. Parry, I. I. Kravchenko, Y.-H. Chen, A. S. Solntsev, Y. S. Kivshar, D. N. Neshev, A. A. Sukhorukov, Quantum metasurface for multiphoton interference and state reconstruction. *Science* **361**, 1104–1107 (2018).
35. T. Roger, S. Vezzoli, E. Bolduc, J. Valente, J. J. F. Heitz, J. Jeffers, C. Soci, J. Leach, C. Couteau, N. I. Zheludev, D. Faccio, Coherent perfect absorption in deeply subwavelength films in the single-photon regime. *Nat. Commun.* **6**, 7031 (2015).
36. T.-Y. Huang, R. R. Grote, S. A. Mann, D. A. Hopper, A. L. Exarhos, G. G. Lopez, G. R. Kaighn, E. C. Garnett, L. C. Bassett, A monolithic immersion metalens for imaging solid-state quantum emitters. *Nat. Commun.* **10**, 2392 (2019).
37. L. Huang, X. Chen, H. Mühlenbernd, G. Li, B. Bai, Q. Tan, G. Jin, T. Zentgraf, S. Zhang, Dispersionless phase discontinuities for controlling light propagation. *Nano Lett.* **12**, 5750–5755 (2012).
38. D. Lin, P. Fan, E. Hasman, M. L. Brongersma, Dielectric gradient metasurface optical elements. *Science* **345**, 298–302 (2014).
39. J. Liu, K. Konthasinghe, M. Davanço, J. Lawall, V. Anant, V. Verma, R. Mirin, S. W. Nam, J. D. Song, B. Ma, Z. S. Chen, H. Q. Ni, Z. C. Niu, K. Srinivasan, Single self-assembled InAs/GaAs quantum dots in photonic nanostructures: The role of nanofabrication. *Phys. Rev. Appl.* **9**, 064019 (2018).
40. Y.-M. He, O. Iff, N. Lundt, V. Baumann, M. Davanco, K. Srinivasan, S. Höfling, C. Schneider, Cascaded emission of single photons from the biexciton in monolayered WSe_2. *Nat. Commun.* **7**, 13409 (2016).

Acknowledgments: We thank S.-I. Park for the help in growing the QDs. **Funding:** This work was supported, in part, by the National Key R&D Program of China (2016YFA0301300), the Key R&D Program of Guangdong Province (grant no. 2018B030329001), the National Natural Science Foundation of China (11804407, 91750207, 11761141015, 11974436, 11761131001, 11674402, 11974437, and 61675237), the Guangdong Basic and Applied Basic Research Foundation (2020B1515020019), the Guangdong Natural Science Foundation (2016A030312012 and 2018A030313333), the Guangzhou Science and Technology Projects (201805010004), the Guangdong Special Support Program (2017TQ04C487), the fundamental research funds for the central universities (19lgpy262 and 19lgjc13), and the National Supercomputer Center in Guangzhou. J.S. acknowledges supports from IITP grant funded by the Korea government (MSIT) (no. 20190004340011001). **Author contributions:** X.-H.W. conceived the idea. Y.B. conducted the structure design and numerical simulation. J.S. grew the QD wafers. Q.L. and R.S. fabricated the samples and performed the measurements. Y.B. wrote the manuscript with input from other authors, and X.-H.W. revised the manuscript. J.L. and X.-H.W. directed the project. All authors analyzed the data and discussed the results. **Competing interests:** The authors declare that they have no competing interests. **Data and materials availability:** All data needed to evaluate the conclusions in the paper are present in the paper and/or the Supplementary Materials. Additional data related to this paper may be requested from the authors.

Submitted 13 January 2020
Accepted 16 June 2020
Published 29 July 2020
10.1126/sciadv.aba8761

Citation: Y. Bao, Q. Lin, R. Su, Z.-K. Zhou, J. Song, J. Li, X.-H. Wang, On-demand spin-state manipulation of single-photon emission from quantum dot integrated with metasurface. *Sci. Adv.* **6**, eaba8761 (2020).